Electrically and magnetically switchable nonlinear photocurrent in $\mathcal{PT}$-symmetric magnetic topological quantum materials

Hua Wang[1] and Xiaofeng Qian[1]*
[1]*Department of Materials Science and Engineering, Texas A&M University, College Station, TX 77843, USA*

*Corresponding author: feng@tamu.edu

Abstract
Nonlinear photocurrent in time-reversal invariant noncentrosymmetric systems such as ferroelectric semimetals sparked tremendous interest of utilizing nonlinear optics to characterize condensed matter with exotic phases. Here we provide a microscopic theory of two types of second-order nonlinear direct photocurrents, magnetic shift photocurrent (MSC) and magnetic injection photocurrent (MIC), as the counterparts of normal shift current (NSC) and normal shift current (NIC) in time-reversal symmetry and inversion symmetry broken systems. We show that MSC is mainly governed by shift vector and interband Berry curvature, and MIC is dominated by absorption strength and asymmetry of the group velocity difference at time-reversed $\pm\boldsymbol{k}$ points. Taking $\mathcal{PT}$-symmetric magnetic topological quantum material bilayer antiferromagnetic (AFM) $MnBi_2Te_4$ as an example, we predict the presence of large MIC in the terahertz frequency regime which can be switched between two AFM states with time-reversed spin orderings upon magnetic transition. In addition, external electric field breaks $\mathcal{PT}$ symmetry and enables large NSC response in bilayer AFM $MnBi_2Te_4$ which can be switched by external electric field. Remarkably, both MIC and NSC are highly tunable under varying electric field due to the field-induced large Rashba and Zeeman splitting, resulting in large nonlinear photocurrent response down to a few THz regime, suggesting bilayer AFM-*z* $MnBi_2Te_4$ as a tunable platform with rich THz and magneto-optoelectronic applications. Our results reveal that nonlinear photocurrent responses governed by NSC, NIC, MSC, and MIC provide a powerful tool for deciphering magnetic structures and interactions which could be particularly fruitful for probing and understanding magnetic topological quantum materials.

Introduction

Magnetic topological quantum materials have attracted a lot of interest as the interplay between magnetic ordering and topology may enable exotic topological quantum states. For example, antiferromagnetic topological insulator[1] can host topological axion states with nonzero quantized Chern-Simons magnetoelectric coupling[2] which was recently predicted in the class of layered $MnBi_2Te_4$ materials[3-5]. The nontrivial topological surface states have been experimentally verified in $MnBi_2Te_4$[6-8]. While various experiments have been carried out to study their electronic structure and transport properties, optical probes, especially nonlinear optical spectroscopy, may provide a rich set of alternative tools to probe their topological nature and understand the inherent electronic structure in these exotic quantum materials.

Nonlinear optical responses play a key role in understanding the symmetry, ordering, and topology. Materials with strong nonlinear responses are particularly valuable for ultrafast nonlinear optics[9], efficient generation of entangled photon pairs[10,11], and phase-matching free nonlinear optics[12,13] using 2D materials. Recently, nonlinear photocurrent responses including normal shift current (NSC)[14-18], normal injection current (NIC)[17-21], and Berry curvature dipole induced current[22-24] have been observed in time-reversal invariant noncentrosymmetric systems. Recently, nonlinear shift current was proposed in centrosymmetric crystals via geometric photon-drag effect[25]. In particular, Berry curvature dipole induced photocurrent is closely coupled with ferroelectric orders, offering a unique approach to detect low-energy ferroelectric transition. This was recently theoretically proposed and experimentally verified in ferroelectric few-layer WTe_2 semimetal, opening avenues to the development of nonlinear quantum memory[24,26]. Compared to few-layer WTe_2, layered $MnBi_2Te_4$ is magnetic with tunable nontrivial topology, which may lead to magnetically and electrically controlled large nonlinear photocurrent responses. The effect of magnetic ordering and intrinsic topology on nonlinear responses in $MnBi_2Te_4$, however, has been largely underexplored.

Here we provide a microscopic theory of two types of second-order nonlinear current responses, namely *magnetic injection current* (MIC) and *magnetic shift current* (MSC), which are the counter part of the well-known NIC and NSC in time-reversal invariant noncentrosymmetric system. Both MIC and MSC can be induced in $\mathcal{PT}$-symmetric systems with space inversion ($\mathcal{P}$) and time reversal ($\mathcal{T}$) being individually broken. We take magnetic topological quantum material bilayer antiferromagnetic (AFM) $MnBi_2Te_4$ as an example of $\mathcal{PT}$-symmetric system and predict that MIC can be switched in time-reversal breaking $MnBi_2Te_4$ upon magnetic transition, namely magnetically switchable nonlinear photocurrent. In addition, vertical electric field breaks $\mathcal{PT}$ symmetry and enables large electrically switchable NSC. Both MIC and NSC are highly tunable owing to field-induced Rashba and Zeeman splitting. Field induced bandgap reduction not only induces topological phase transition of bilayer AFM $MnBi_2Te_4$ from zero-plateau quantum anomalous Hall insulator into high Chern number quantum anomalous Hall insulator, but also leads to large nonlinear photocurrent response redshifted down to a few THz regime, suggesting $MnBi_2Te_4$ may serve as a promising platform for terahertz sensing and magneto-optoelectronic applications. The rich nonlinear photocurrent responses in time-reversal and inversion symmetry broken systems are inherently coupled with their crystal structure and magnetic symmetry, offering a promising route for probing and understanding the intrinsic electronic structure and potentially topological physics in magnetic quantum materials.

Results

Microscopic theory of second-order nonlinear photocurrent

General second-order direct injection current (IC) and shift current (SC) under monochromatic electric field $E^b(t) = E^b(\omega_\beta)e^{-i\omega_\beta t}$ with $\omega_\beta = \pm\omega$ in the clean limit are given by [14,17,27]

$$\frac{dJ^a_{\text{IC}}}{dt} = -\frac{\pi e^3}{\hbar^2}\int [d\mathbf{k}] \sum_{mn\sigma} f_{mn}\Delta^a_{mn} r^b_{nm} r^c_{mn}\, \delta(\omega_{nm} - \omega_\beta) E^b(\omega_\beta) E^c(-\omega_\beta), \tag{1}$$

$$J^a_{\text{SC}} = -\frac{i\pi e^3}{2\hbar^2}\int [d\mathbf{k}] \sum_{mn\sigma} f_{nm}\left(r^b_{mn} r^c_{nm;k^a} - r^c_{nm} r^b_{mn;k^a}\right)\delta(\omega_{nm} - \omega_\beta) E^b(\omega_\beta) E^c(-\omega_\beta), \tag{2}$$

where a, b, c are Cartesian indices, $r^b_{mn;k^a} = \frac{\partial r^b_{mn}}{\partial k^a} - i r^b_{mn}(\mathcal{A}^a_m - \mathcal{A}^a_n)$ is the gauge covariant derivative. $\boldsymbol{r}_{nm} = i\langle n|\partial_{\boldsymbol{k}}|m\rangle$ and $\boldsymbol{\mathcal{A}}_n = i\langle n|\partial_{\boldsymbol{k}}|n\rangle$ are interband and intraband Berry connection, respectively. f_m is the Fermi-Dirac distribution with $f_{nm} \equiv f_n - f_m$, and $\hbar\Delta^a_{mn} \equiv v^a_{mm} - v^a_{nn}$ is the group velocity difference of band m and n. $[d\mathbf{k}] \equiv \frac{d\mathbf{k}}{(2\pi)^d}$ for d-dimension. Here $e = -|e|$ carries a negative sign due to the negative charge of electron. We separate the product of the electric field amplitude into the symmetric real and antisymmetric imaginary parts,

$$E^b(\omega)E^c(-\omega) = E^b(\omega)E^{c*}(\omega) = \text{Re}\left(E^b E^{c*}\right) + i\text{Im}\left(E^b E^{c*}\right), \tag{3}$$

$$E^b(-\omega)E^c(\omega) = E^{b^*}(\omega)E^c(\omega) = \text{Re}\left(E^b E^{c*}\right) - i\text{Im}\left(E^b E^{c*}\right). \tag{4}$$

For linearly polarized light, $\boldsymbol{E}(\omega)$ is real, while for left/right-circularly polarized light $\boldsymbol{E}(\omega)$ is complex with $\text{Im}\, E^b(\omega)E^c(-\omega) = -\text{Im}\, E^b(-\omega)E^c(\omega) \neq 0$. After symmetrization with $\pm\omega$, we have

$$\frac{dJ^a_{\text{IC}}}{dt} = -\frac{\pi e^3}{\hbar^2}\int [d\mathbf{k}] \sum_{mn\sigma} f_{mn}\Delta^a_{mn}\{r^b_{nm}, r^c_{mn}\}\, \delta(\omega_{nm} - \omega)\ \text{Re}\left(E^b E^{c^*}\right)$$

$$-i\frac{\pi e^3}{\hbar^2}\int [d\mathbf{k}] \sum_{mn\sigma} f_{mn}\Delta^a_{mn}[r^b_{nm}, r^c_{mn}]\, \delta(\omega_{nm} - \omega)\ \text{Im}\left(E^b E^{c^*}\right), \tag{5}$$

where $\{r^b_{nm}, r^c_{mn}\} \equiv r^b_{nm} r^c_{mn} + r^c_{nm} r^b_{mn}$, and $[r^b_{nm}, r^c_{mn}] \equiv r^b_{nm} r^c_{mn} - r^c_{nm} r^b_{mn}$. We then arrive at

$$\frac{dJ^a_{\text{IC}}}{dt} = 2\eta^{abc}_{\text{MIC}}\, \text{Re}\left(E^b E^{c*}\right) + 2i\eta^{abc}_{\text{NIC}}\, \text{Im}\left(E^b E^{c*}\right), \tag{6}$$

where

$$\eta^{abc}_{\text{NIC}} = -\frac{\pi e^3}{2\hbar^2}\int [d\mathbf{k}] \sum_{mn\sigma} f_{mn}\, \Delta^a_{mn}[r^b_{nm}, r^c_{mn}]\, \delta(\omega_{nm} - \omega)\ , \tag{7}$$

$$\eta^{abc}_{\text{MIC}} = -\frac{\pi e^3}{2\hbar^2}\int [d\mathbf{k}] \sum_{mn\sigma} f_{mn}\, \Delta^a_{mn}\{r^b_{nm}, r^c_{mn}\}\, \delta(\omega_{nm} - \omega)\, , \tag{8}$$

η^{abc}_{NIC} is the well-known NIC susceptibility, which vanishes under linearly polarized light. η^{abc}_{MIC} is an additional term, MIC susceptibility, arising from our microscopic derivation, which recovers the same formula as Yan's work[28]. It's clear that $\eta_{\rm MIC}^{abc}=0$ under time-reversal symmetry. Detailed derivation of nonlinear photocurrent responses using density matrix formalism can be found in Supplementary Note 1.

Similarly, we can separate shift current into the well-known NSC and an additional term - MSC:

$$J_{\rm SC}^a = J_{\rm NSC}^a + J_{\rm MSC}^a = 2\sigma_{\rm NSC}^{abc}\,{\rm Re}\left(E^b E^{c*}\right) + 2i\sigma_{\rm MSC}^{abc}\,{\rm Im}\left(E^b E^{c*}\right) \tag{9}$$

where

$$\sigma_{\rm NSC}^{abc} = -\frac{i\pi e^3}{4\hbar^2}\int[d\mathbf{k}]\sum_{mn\sigma} f_{nm}\left(r_{mn}^b r_{nm;k^a}^c + r_{mn}^c r_{nm;k^a}^b\right)\left(\delta(\omega_{nm}-\omega)+\delta(\omega_{mn}-\omega)\right), \tag{10}$$

$$\sigma_{\rm MSC}^{abc} = -\frac{i\pi e^3}{4\hbar^2}\int[d\mathbf{k}]\sum_{mn\sigma} f_{nm}\left(r_{mn}^b r_{nm;k^a}^c - r_{mn}^c r_{nm;k^a}^b\right)\left(\delta(\omega_{nm}-\omega)-\delta(\omega_{mn}-\omega)\right). \tag{11}$$

Under time-reversal symmetry, the NSC and MSC susceptibilities can be rewritten in a compact form as follows,

$$\sigma_{\rm NSC}^{abc} = -\frac{\pi e^3}{4\hbar^2}\int[d\mathbf{k}]\sum_{mn\sigma} f_{nm}\left(R_{mn}^{a,b}(\mathbf{k}) + R_{mn}^{a,c}(\mathbf{k})\right)\{r_{nm}^b, r_{mn}^c\}\delta(\omega_{nm}-\omega), \tag{12}$$

$$\sigma_{\rm MSC}^{abc} = -\frac{\pi e^3}{4i\hbar^2}\int[d\mathbf{k}]\sum_{mn\sigma} f_{nm}\left(R_{mn}^{a,b}(\mathbf{k}) + R_{mn}^{a,c}(\mathbf{k})\right)\Omega_{mn}^d(\mathbf{k})\delta(\omega_{nm}-\omega) \tag{13}$$

where $R_{mn}^{a,b}(\mathbf{k}) = -\frac{\partial\phi_{mn}^b(\mathbf{k})}{\partial k^a} + \mathcal{A}_m^a(\mathbf{k}) - \mathcal{A}_n^a(\mathbf{k})$ is shift vector and $\phi_{nm}(\mathbf{k})$ is the phase factor of the interband Berry connection $r_{nm}^b(\mathbf{k}) = \left|r_{nm}^b(\mathbf{k})\right|e^{i\phi_{nm}^b(\mathbf{k})}$ and $\Omega_{mn}^d = i\epsilon_{dbc} r_{mn}^b r_{nm}^c = i\left(r_{mn}^b r_{nm}^c - r_{mn}^c r_{nm}^b\right)$ is the local Berry curvature between band *m* and *n*. As indicated by Levi-Civita tensor ϵ_{dbc}, the direction of light propagation for MSC is along *d*, *i.e.* along $(E^b\times E^c)$, The MSC is vanishing in time-reversal invariant system since Berry curvature Ω_{mn}^a is an odd function and shift vector is even function with **k** under time-reversal symmetry. MSC can be induced by circularly polarized light in gyrotropic magnetic materials. During the preparation of this manuscript, we noticed that another paper[29] by de Juan derived an equivalent equation using the similar density matrix approach and Fei *et al.*[30] also proposed giant linearly polarized photogalvanic effect using a diagrammatic approach which is equivalent to MIC. In the present study, bilayer $MnBi_2Te_4$ is non-gyrotropic, hence it has vanishing MSC. Nevertheless, MSC in gyrotropic magnetic materials is worth for a further exploration which is closely related to magnetic bulk phototactic.[31] It should be noted that the term of "magnetic" nonlinear current defined in the MSC and MIC in Eq. (8) and Eq. (11) is different from conventional spin current. Instead, it refers to the charge current which is present in magnetic materials but vanishes in intrinsic nonmagnetic materials. Furthermore, we can extend the above nonlinear shift and injection current to nonlinear shift spin current and nonlinear injection spin current by substituting the current operator $j^{a(s_b)} = -ev_a \to \frac{1}{2}\{s_b, v_a\}$, where $s_b = \frac{\hbar}{2}\sigma_b$ is spin operator with Pauli matrices σ_b. The extended nonlinear photo-spin current responses provide an essential route for exploring spin physics in condensed matter, which is currently under exploration and out of the scope in the present work.

Crystal structure and group theory of bilayer $MnBi_2Te_4$

Here we present a magnetic group theoretical analysis of bilayer AFM-*z* $MnBi_2Te_4$ (Fig. 1a and 1c) with interlayer antiferromagnetic ordering of the Mn atoms aligned along the *z* direction, while group theoretical analysis of bilayer $MnBi_2Te_4$ with different magnetic orderings can be found in Supplementary Note 2. In general, the dichromatic group $\mathcal{M}$ can be constructed by $\mathcal{M} = \mathcal{G}(\mathcal{H}) = \mathcal{H} \oplus (\mathcal{G} - \mathcal{H})\mathcal{T}$ where $\mathcal{G}$ is the ordinary geometric point group, $\mathcal{H}$ is the subgroup of $\mathcal{G}$ of index 2, and $\mathcal{T}$ is time-reversal operator. As a result, magnetic point group of bilayer AFM-*z* $MnBi_2Te_4$ is $\bar{3}'m' = D_{3d}(D_3) = \{E, 2C_3, 3C_2', i\mathcal{T}, 2S_6\mathcal{T}, 3\sigma_d\mathcal{T}\}$. The character table of point group D_{3d} is included in Supplementary Table S1. Without considering the ordering of spin, bilayer $MnBi_2Te_4$ is centrosymmetric with vanishing second-order nonlinear current responses. Taking into account the AFM-*z* structure, $\mathcal{PT}$ symmetry is preserved in bilayer $MnBi_2Te_4$ with individual $\mathcal{P}$ and $\mathcal{T}$ symmetry being broken. In addition, as shown in Fig. 1b, bilayer AFM-*z* $MnBi_2Te_4$ holds a two-fold rotation symmetry along *x*-axis $C_{2x} = \mathcal{M}_y\mathcal{M}_z$, and a combination of mirror symmetry and time-reversal symmetry $\mathcal{M}_x\mathcal{T}$.

For systems holding magnetic point group $\bar{3}'m'$ (such as bilayer and bulk AFM-*z* $MnBi_2Te_4$), both normal magnetoelectric coupling and topological axion coupling are symmetry allowed. The polar *i*-vectors (*i.e.* time-reversal symmetric and space-inversion antisymmetric vector), e.g., electric field $\boldsymbol{E}$ or electric polarization $\boldsymbol{P}$, are represented by $\mathrm{A}_{2u}(z)$ and $\mathrm{E}_u(x, y)$ in D_{3d} group and they are time-reversal symmetric but space-inversion antisymmetric. $\mathrm{A}_{2g}(R_z)$ and $\mathrm{E}_g(R_x, R_y)$ represent axial *i*-vectors which are symmetric under both time reversal and space inversion. The general transformation of polar/axial *i*-/*c*-tensors under space inversion $\mathcal{P}$, time-reversal operation $\mathcal{T}$, and $\mathcal{PT}$ can be found in Supplementary Table S2. We can see the two types of vectors are incompatible in D_{3d} group, e.g., $\mathrm{A}_{2u}\otimes\mathrm{A}_{2g} = \mathrm{A}_{1u}$ does not contain total symmetric A_{1g}. The magnetic field $\boldsymbol{B}$ or orbital magnetization $\boldsymbol{M}$ are axial *c*-vectors which are time-reversal antisymmetric but space-inversion symmetric.

For magnetic point groups, we use Birss's notation [32], where Γ_s is the total symmetric representation, Γ_m is the one-dimensional representation that corresponds to $\mathcal{M}$ in which all elements of $\mathcal{H}$ are represented by +1, and Γ_p is the pseudovector representation in group $\mathcal{G}$. We shall write the direct product representation $\Gamma_{m\otimes p} = \Gamma_m \otimes \Gamma_p$ for axial *c*-vector. For magnetic point group $D_{3d}(D_3)$, we have $\Gamma_s = A_{1g}, \Gamma_m = A_{1u}, \Gamma_p = A_{2g} + E_g$. Thus, $\Gamma_{m\otimes p} = A_{2u} + E_u$. Consequently, $\Gamma_{\boldsymbol{M}} \otimes \Gamma_{\boldsymbol{E}} = \Gamma_{\boldsymbol{P}} \otimes \Gamma_{\boldsymbol{B}} = 2A_{1g} + A_{2g} + 3E_g$. Hence, the linear magnetoelectric coupling of $\bar{3}'m'$ structures has two independent nonvanishing components and corresponding orbital magnetoelectric polarizability. Now let's see how *c*-type second-order current response under linearly polarized light such as MIC is enabled in $D_{3d}(D_3)$ by considering the following direct product $\Gamma_m \otimes \Gamma_{\boldsymbol{j}} \otimes (\Gamma_{\boldsymbol{E}} \otimes \Gamma_{\boldsymbol{E}})^s = A_{1g} + 3A_{2g} + 4E_g$, indicating only one independent and nonvanishing susceptibility is allowed. For *i*-type second-order current response under linearly polarized light such as NSC, we have the direct product: $\Gamma_{\boldsymbol{j}} \otimes (\Gamma_{\boldsymbol{E}} \otimes \Gamma_{\boldsymbol{E}})^s = (A_{2u} + E_u) \otimes \left(2A_{1g} + E_g\right) = A_{1u} + 3A_{2u} + 4E_u$. Hence, NSC is not symmetry allowed. In fact, NSC is immune to the time reversal symmetry and can be determined by nonmagnetic point group. As bilayer/bulk $MnBi_2Te_4$ holds nonmagnetic point group D_{3d} with inversion symmetry, both NSC and NIC vanish. Similarly, *c*-type second-order current response under circularly polarized light such as MSC is forbidden in $D_{3d}(D_3)$ by considering the following direct product: $\Gamma_m \otimes \Gamma_{\boldsymbol{j}} \otimes \Gamma_{\boldsymbol{E}\times\boldsymbol{E}^*} = 2A_{1u} + A_{2u} + 3E_u$ which does not contain total symmetric representation. The above analysis can be extended to other higher order optical/photocurrent responses in magnetic materials.

Nonlinear photocurrent in bilayer $MnBi_2Te_4$

Ground-state crystal structures of $MnBi_2Te_4$ were calculated using first-principles density-functional theory[33,34] implemented in the Vienna Ab initio Simulation Package (VASP)[35,36] with the projector-augmented wave method[37]. We then performed first-principles calculations of nonlinear photocurrent including MIC and NSC. Specifically, with the fully relaxed ground-state crystal structure, we constructed quasiatomic spinor Wannier functions and tight-binding Hamiltonian from Kohn-Sham wavefunctions and eigenvalues under the maximal similarity measure with respect to pseudoatomic orbitals[38,39]. Using the developed tight-binding Hamiltonian, we then computed MIC and NSC susceptibility tensor using a modified WANNIER90 code[40] with a k-point grid of 1000×1000×1. Spin-orbit coupling was taken into account. More details can be found in the Methods section.

Figure 2a and 2b present the electronic structure and MIC susceptibility η_{MIC}^{xxx} in bilayer $MnBi_2Te_4$ with magnetic ordering in AFM-*z* (↑↓) and time-reversed AFM-*z* (tAFM-*z*, ↓↑), respectively. The corresponding magnetic ordering is shown in Fig. 2a inset. The $\boldsymbol{k}$-space distribution of $f_{mn}\Delta_{mn}^{a}\{r_{nm}^{b}, r_{mn}^{c}\}\delta(\omega_{nm}-\omega)$ with a unit of Å^3 at $\omega = 120$ meV and $\omega = 600$ meV are shown in Figure 2c and 2d for bilayer AFM-*z* and in Fig. 2e and 2f for tAFM-*z* $MnBi_2Te_4$, respectively. This term arises from the large difference of the asymmetric group velocity Δ_{mn}^{a} and the absorption strength $\{r_{nm}^{b}, r_{mn}^{c}\}$ at time-reversed $\pm\boldsymbol{k}$ points, which eventually contributes to the large MIC in bilayer AFM-*z* and tAFM-*z* $MnBi_2Te_4$. The peak MIC conductivity is $\sim 2\times 10^{10}\ \text{nm}\cdot\text{A}\cdot\text{V}^{-2}\cdot\text{s}^{-1}$, two times the peak NIC in ferroelectric monolayer GeS [17]. More importantly, it demonstrates that the MIC can be switched upon magnetic ordering transition between AFM-*z* (↑↓) and its time-reversed tAFM-*z* (tAFM, ↓↑) configurations. With additional three-fold rotation symmetry, we have $\eta_{\text{MIC}}^{xxx} = -\eta_{\text{MIC}}^{xyy} = -\eta_{\text{MIC}}^{yxy} = -\eta_{\text{MIC}}^{yyx}$. Moreover, the presence of $\mathcal{M}_y\mathcal{M}_z$ symmetry leads to vanishing η_{MIC}^{yyy}. The switching of MIC for bilayer AFM-*z* and tAFM-*z* MBT can be understood from a symmetry analysis. The MIC is determined by the integral of $f_{mn}\,\Delta_{mn}^{a}\{r_{nm}^{b}, r_{mn}^{c}\}\,\delta(\omega_{nm}-\omega)$ in the Brillouin zone. Under time-reversal operation, we have

$$\mathcal{T}\sum_{mn\boldsymbol{k}} f_{mn}(\boldsymbol{k})\Delta_{mn}^{a}(\boldsymbol{k})\{r_{nm}^{b}(\boldsymbol{k}), r_{mn}^{c}(\boldsymbol{k})\}\,\delta\big(\omega_{nm}(\boldsymbol{k})-\omega(\boldsymbol{k})\big)$$

$$= -\sum_{mn-\boldsymbol{k}} f_{mn}(-\boldsymbol{k})\,\Delta_{mn}^{a}(-\boldsymbol{k})\{r_{nm}^{b}(-\boldsymbol{k}), r_{mn}^{c}(-\boldsymbol{k})\}\,\delta\big(\omega_{nm}(-\boldsymbol{k})-\omega(-\boldsymbol{k})\big)$$

$$= -\sum_{mn\boldsymbol{k}} f_{mn}(\boldsymbol{k})\,\Delta_{mn}^{a}(\boldsymbol{k})\{r_{nm}^{b}(\boldsymbol{k}), r_{mn}^{c}(\boldsymbol{k})\}\,\delta\big(\omega_{nm}(\boldsymbol{k})-\omega(\boldsymbol{k})\big) \tag{14}$$

Hence, MIC switches the sign in the AFM-*z* and tAFM-*z* MBT.

Van der Waals layered $MnBi_2Te_4$ hosts rich topology with varying magnetic orders that are different from the above AFM-*z* structure (Supplementary Table S3), subsequently the corresponding nonlinear current responses can be very different. For example, FM-*x* and FM-*z* magnetic ordering under external magnetic field (*i.e.* ferromagnetic ordering with magnetization aligned along *x*/*z* direction) holds inversion symmetry, hence has vanishing even-order nonlinear optical and photocurrent responses including SHG, NSC, NIC, MSC, and MIC. Supplementary Figure S1 shows the band structure for the FM-z magnetic ordering where each band is symmetric with respect to ±$\boldsymbol{k}$ points with vanishing MIC. In addition, for bilayer $MnBi_2Te_4$ with AFM-*x* magnetic ordering, the corresponding magnetic point group becomes $2'/m = C_{2h}(C_s) = C_s \oplus (C_{2h}-C_s)\mathcal{T} = \{E, \sigma_x, C_{2x}\mathcal{T}, i\mathcal{T}\}$, different from $\overline{3}'m'$ for bilayer $MnBi_2Te_4$ with

AFM-z magnetic structure. Nonetheless, bilayer AFM-x $MnBi_2Te_4$ preserves $\mathcal{PT}$-symmetry and allows for nonvanishing MIC response $\eta_{\mathrm{MIC}}^{xxy}$, $\eta_{\mathrm{MIC}}^{yxx}$ and $\eta_{\mathrm{MIC}}^{yyy}$ as shown in Supplementary Figure S2. It is worth to point out that van der Waals layered $MnBi_2Te_4$ hosts rich topology with varying magnetic ordering. Probing MIC response can, therefore, help directly determine the intrinsic magnetic structure and hence potential topology of magnetic topological quantum materials owing to the intimate coupling between magnetic symmetry and nonlinear photocurrent responses.

Normal shift current in electrically-gated bilayer $MnBi_2Te_4$

Although both bilayer AFM-z and tAFM-z $MnBi_2Te_4$ hold the large MIC response as shown above, their Berry curvature $\Omega_n(\boldsymbol{k})$ and shift vector $R_{mn}^{a}(\boldsymbol{k})$ are vanishing due to $\mathcal{PT}\Omega_n(\boldsymbol{k}) = -\Omega_n(\boldsymbol{k}) = \Omega_n(\boldsymbol{k})$ and $\mathcal{PT}R_{mn}^{a}(\boldsymbol{k}) = -R_{mn}^{a}(\boldsymbol{k}) = R_{mn}^{a}(\boldsymbol{k})$. Hence, no NSC and Berry curvature related physics would be expected in $\mathcal{PT}$-symmetric system. In fact, one can take the wave functions to be real (due to the $\mathcal{PT}$ transformation). Then the phase effect is absent and the shift vector and Berry curvature become zero in $\mathcal{PT}$-symmetric system. However, one can apply Berry curvature engineering via electric gating to break the $\mathcal{PT}$ symmetry symmetry in the pristine bilayer $MnBi_2Te_4$ [41]. Here we apply an external electric field along the out of plane direction to bilayer $MnBi_2Te_4$. Figure 3a and 3b show the calculated electronic structure and NSC in bilayer $MnBi_2Te_4$ under an external electric field $E_z = 10\ \mathrm{mV}\cdot\text{Å}^{-1}$ with magnetic ordering AFM-z (↑↓). Large Rashba and Zeeman spin splitting are indicated in Fig. 3a which we will discuss soon. The peak NSC conductivity is $\sim 1000\ \mathrm{nm}\cdot\mu\mathrm{A}\cdot\mathrm{V}^{-2}$, which is 50 times larger than that in GeS[17]. In addition, Figure 3c-f present the microscopic distribution of NSC, $\sum_{mn\sigma} f_{nm}\left(r_{mn}^{b} r_{nm;k^a}^{c} + r_{mn}^{c} r_{nm;k^a}^{b}\right)\left(\delta(\omega_{nm}-\omega) + \delta(\omega_{mn}-\omega)\right)$, with a unit of $\text{Å}^3\cdot(eV)^{-1}$ at two frequencies ($\omega = 60$ meV and $\omega = 115$ meV) in bilayer AFM-z with $E_z = \pm 10\ \mathrm{mV}\cdot\text{Å}^{-1}$. From the symmetry transformation $\mathcal{M}_y\mathcal{M}_z E_z = -E_z$, we can see that the direction of NSC along y under linearly y-polarized light can be flipped by switching the electric field from +z to -z. The external electric field of $10\ \mathrm{mV}\cdot\text{Å}^{-1}$ is feasible for few-layer 2D materials when the thickness is on the order of ~nm. Recently, Xiao et al. measured nonlinear anomalous Hall effect in trilayer and four-layer WTe_2 using an electric field up to ~$40\ \mathrm{mV}\cdot\text{Å}^{-1}$.[26] Similar to MIC, NSC, and NIC, nonlinear anomalous Hall effect is also originated from a type of second-order nonlinear current responses due to the intraband Berry curvature dipole. We therefore expect that it may be possible to carry out experimental measurement of MIC using an electric field of ~$10\ \mathrm{mV}\cdot\text{Å}^{-1}$.

Similar to the case of MIC, $\sigma_{\mathrm{NSC}}^{yyy} = -\sigma_{\mathrm{NSC}}^{yxx} = -\sigma_{\mathrm{NSC}}^{xyx} = -\sigma_{\mathrm{NSC}}^{xxy}$ under three-fold rotation symmetry, and $\sigma_{\mathrm{NSC}}^{xxx}$ vanishes due to $\mathcal{M}_x\mathcal{T}$ symmetry. It's important to realize that upon linearly polarized incident light along x direction, the response of NSC in the electrically gated bilayer AFM-z and tAFM-z $MnBi_2Te_4$ is governed by $\sigma_{\mathrm{NSC}}^{yxx}$ with nonlinear photocurrent generated along y only. In contrast, under the same linearly x-polarized light, the response of MIC is dominated by $\eta_{\mathrm{MIC}}^{xxx}$ with nonlinear photocurrent generated along x only. Moreover, NSC does not switch in bilayer AFM-z (↑↓) and time-reversed AFM-z (tAFM, ↓↑) $MnBi_2Te_4$, indicating that NSC cannot be reversed under $\mathcal{T}$ corresponding to its dissipative and non-reciprocal nature [42]. In addition, as aforementioned, NSC vanishes when electric field is absent, while MIC always exists regardless of electric field. As shown in Fig. 2 and Fig. 3, both NSC and MIC in bilayer AFM-z $MnBi_2Te_4$ have strong responses at low energy regime (e.g. two strong NSC peaks at 60 meV and 115 meV under $E_z = 10\ \mathrm{mV}\cdot\text{Å}^{-1}$ and two strong MIC peaks at 120 meV and 600 meV), making them particularly attractive for terahertz and infrared sensing.

Tunable nonlinear photocurrent in bilayer $MnBi_2Te_4$

Both NSC and MIC are highly tunable under varying electric field. Figure 4a shows the electric field dependent band structure. The band gap decreases upon increasing vertical electric field until a critical field of $E_z = 25\ \mathrm{mV} \cdot \text{Å}^{-1}$ where it undergoes topological phase transition from zero-plateau quantum anomalous Hall insulator with Chern number $C_n = 0$ to high Chern number quantum anomalous Hall insulator ($C_n = 3$). The nontrivial topology is evinced in the Berry curvature shown in Fig. 4b which is localized around the center of the Brillouin zone. The integration of Berry curvature yields a high Chern number of $C_n = 3$. As aforementioned, electric field can introduce large Rashba and Zeeman splitting in bilayer AFM-*z* $MnBi_2Te_4$. In Fig. 4c and 4d we show the corresponding spin polarization at the energy of 0.6 eV with AFM-*z* and tAFM-*z* magnetic ordering under a vertical electric field of $E_z = 10\ \mathrm{mV} \cdot \text{Å}^{-1}$, which confirms large spin splitting with three-fold rotation symmetry under finite electric field. Under the same electric field, spin polarization in AFM-*z* and tAFM-*z* are related by time reversal $\mathcal{T}$ operation. However, for the same magnetic configuration AFM-*z* or tAFM-*z*, the spin polarization under electric field along +z and -z are related by $\mathcal{PT}$ operation (see Supplementary Figure S3). Electric field induced large spin splitting and distinct spin polarization suggest that bilayer AFM-*z* $MnBi_2Te_4$ could serve as a rich platform for developing electrically controlled spintronics.

Electric field induced Rashba and Zeeman splitting reduces the electronic gap, thereby shifting the nonlinear photocurrent responses such as MIC and NSC to the THz regime. Figure 4e and 4f show field-dependent NSC and MIC responses in bilayer AFM-*z* $MnBi_2Te_4$ under varying electric field. It clearly demonstrates that the strength of NSC response increases under increasing electric field until $E_z = 23\ \mathrm{mV} \cdot \text{Å}^{-1}$, and the MIC conductibility remains very large until $E_z = 23\ \mathrm{mV} \cdot \text{Å}^{-1}$. More importantly, the low-energy peak of NSC and MIC response linearly decreases to ~25 meV upon increasing field up to $E_z = 23\ \mathrm{mV} \cdot \text{Å}^{-1}$. It's worth to point out that NSC will switch the sign upon the switching of electric field from +*z* to -*z*, however the sign of MIC will remain the same. This is another way to distinguish NSC and MIC. We would like to mention that the NSC and MIC calculated here is solely contributed by bulk response. Topologically protected edge states in QAHI will also contribute nonlinear current responses, which is outside the scope of this work and needs to be explored in future.

Discussion

The distinct directional dependence and switching behavior of NSC and MIC under different electric field and magnetic ordering provide a fundamental basis to distinguish these two current responses in experiment. First, as shown above, under linearly polarized light, MIC can be generated in $\mathcal{PT}$-symmetric system such as bilayer AFM-*z* $MnBi_2Te_4$. NSC, though absent in the $\mathcal{PT}$-symmetric system, can be enabled via electric gating. Moreover, for electrically gated bilayer AFM-*z* and tAFM-*z* $MnBi_2Te_4$ under linearly *x*-polarized light, NSC susceptibility tensor element $\sigma_{\mathrm{NSC}}^{yxx}$ contributes a large nonlinear photocurrent along *y* only, while MIC susceptibility tensor element $\eta_{\mathrm{MIC}}^{xxx}$ contributes a large nonlinear photocurrent along *x* only. More importantly, nonlinear photocurrent from NSC can be switched by applying vertical electric field along +*z*/-*z* direction, while nonlinear photocurrent from MIC can be reversed by inducing magnetic transition between AFM-*z* and tAFM-*z*. Furthermore, different magnetic orderings (e.g. AFM-*z*, AFM-*x*, FM-*z*, and FM-*x*) yield distinct magnetic point group, thus different directional dependence of nonlinear photocurrent. Such rich coupling between the magnetic ordering and nonlinear photocurrent responses presents itself a powerful tool for investigating magnetic symmetries, structures, and interactions in magnetically ordered crystals as well as imaging magnetic domain walls.

Bilayer AFM-*z* $MnBi_2Te_4$ possesses large MIC and NSC that are highly tunable under electric field with the first low-energy peak red-shifted down to 25 meV (*i.e.* ~6 THz), offering a promising platform for THz sensing of extreme nonlinear quantum phenomena. The large MIC response is originated from the large absorption strength and asymmetry of the group velocity difference at time-reversed $\pm \boldsymbol{k}$ points due to the breaking of time reversal symmetry. The large NSC response comes from the strong absorption strength and the large shift vector which is related to large inter-band Berry curvature. Topological insulators including the MBT studied here usually have small bandgap and large inter-band transition matrix elements and large Berry curvature, which is expected for most magnetic topological insulators with symmetry-allowed nonlinear photocurrent. $\mathcal{PT}$ symmetry plays an important role in the present case, and it is also crucial for non-Hermitian magnetic structures with balanced gain and loss[43]. In addition to MIC and NSC, MSC presents another interesting second order photocurrent response which vanishes in time-reversal invariant systems. MSC can be induced by circularly polarized light in gyrotropic magnetic materials. Furthermore, nonlinear shift and injection current can be extended to nonlinear shift spin current and nonlinear injection spin current, yielding nonlinear photo-spin current response. This will provide an essential route for exploring spin physics in condensed matter, which is currently under exploration and out of the scope in the present work.

In summary, the intimate coupling between intrinsic magnetic point group and nonlinear optical/photocurrent responses makes nonlinear spectroscopy and imaging a powerful tool for investigating magnetic symmetries, structures and interactions in magnetically ordered crystals. In particular, we predicted that $\mathcal{PT}$-symmetric magnetic topological quantum material bilayer $MnBi_2Te_4$ possesses large, magnetically switchable MIC in the THz regime. Although NSC vanishes in $\mathcal{PT}$ symmetric system, electric field breaks the $\mathcal{PT}$-symmetry in bilayer AFM-*z* $MnBi_2Te_4$, and enables large NSC response at the IR regime. More importantly, NSC can be switched by vertical electric field and MIC be switched upon magnetic transition, however NSC (MIC) will not be switched by magnetic transition (electric field). Due to the magnetic group symmetry of bilayer AFM-*z* $MnBi_2Te_4$, MIC and NSC yield photocurrent that are perpendicular to each other upon linearly *x/y*-polarized light, hence can be distinguished. Very excitingly, electric gating can efficiently tune the large nonlinear photocurrent response down to 6 THz, suggesting bilayer AFM-*z* $MnBi_2Te_4$ as an exciting platform for THz and magneto-optoelectronic applications as well as 2D spintronics that are electrically and magnetically tunable. The present work reveals that nonlinear photocurrent responses governed by NSC, NIC, MSC, and MIC provide a powerful spectroscopic/imaging tool for the investigation of magnetic structures and interactions which could be particularly fruitful for probing and understanding magnetic topological quantum materials.

Methods

Ground state crystal and electronic structure. Ground-state crystal structures of $MnBi_2Te_4$ were calculated using first-principles density-functional theory[33,34] implemented in the Vienna Ab initio Simulation Package (VASP)[35,36] with the projector-augmented wave method[37] and a plane-wave basis with an energy cutoff of 400 eV. We employed the generalized-gradient approximation of exchange-correlation energy functional in the Perdew-Burke-Ernzerhof [44] form. A Hubbard U correction with U= 4 eV was applied to Mn atoms to reduce the self-interaction error present in DFT-PBE. We further adopted a Monkhorst-Pack k-point sampling of 11×11×1 for the Brillouin zone integration and DFT-D3 functional[45] to account for weak interlayer dispersion interactions. The convergence criteria for maximal residual force was set to 0.005 eV $Å^{-1}$, and the convergence criteria for electronic relaxation was set to 10^{-6} eV.

First-principles calculations of nonlinear photocurrent. With the fully relaxed ground-state crystal structure, we constructed quasiatomic spinor Wannier functions and tight-binding Hamiltonian from Kohn-Sham wavefunctions and eigenvalues under the maximal similarity measure with respect to pseudoatomic orbitals[38,39]. Spin-orbit coupling was taken into account. Total 120 quasiatomic spinor Wannier functions were obtained from the projections onto Mn's *s* and *d* pseudo-atomic orbitals, Te's *s* and *p* pseudo-atomic orbitals, and Bi's *s* and *p* pseudo-atomic orbitals for bilayer $MnBi_2Te_4$. Using the developed tight-binding Hamiltonian, we then computed MIC and NSC susceptibility tensor using a modified WANNIER90 code[40]. A small imaginary smearing factor η of 5 meV was applied to fundamental frequency. A k-point grid of 1000×1000×1 was adopted, which is dense enough to reach the convergence as shown in Supplementary Figure S4. Tight-binding Hamiltonian was not directly symmetrized, however we carefully inspect the resulted electronic structure by comparing the calculated band structures with the recent publications by Li et al.[4] and Du et al. [41] and our calculations are in good agreement with their results. Second, the electronic band structure of bilayer AFM-z MBT (Figure 1d) and the contour plot of the energy difference between bottom conduction band and top valence (Figure 1e) demonstrate the presence of $\mathcal{PT}$ and C_3 symmetries.

Data availability

The datasets generated during and/or analyzed during the current study are available from the corresponding author on reasonable request.

Acknowledgements

We thank Yong Xu, Shiqiao Du, and Takahiro Morimoto for helpful discussions. This work was supported by the National Science Foundation (NSF) under award number DMR-1753054 and Texas A&M University President's Excellence Fund X-Grants Program. Portions of this research were conducted with the advanced computing resources provided by Texas A&M High Performance Research Computing.

Author contributions

X.Q. conceived the project. H.W. developed first-principles code for magnetic injection current susceptibility and carried out the calculations. H.W. and X.Q. conducted theoretical analysis, analyzed the results, and wrote the manuscript.

Additional information

Supplementary information is available.

Competing interests: The authors declare no competing interests.

References

1 Mong, R. S., Essin, A. M. & Moore, J. E. Antiferromagnetic topological insulators. *Phys. Rev. B* **81**, 245209 (2010).

2 Qi, X.-L., Hughes, T. L. & Zhang, S.-C. Topological field theory of time-reversal invariant insulators. *Phys. Rev. B* **78**, 195424 (2008).

3 Zhang, D. *et al.* Topological Axion States in the Magnetic Insulator $MbBi_2Te_4$ with the Quantized Magnetoelectric Effect. *Phys. Rev. Lett.* **122**, 206401 (2019).

4 Li, J. *et al.* Intrinsic magnetic topological insulators in van der Waals layered $MnBi_2Te_4$-family materials. *Sci. Adv.* **5**, eaaw5685 (2019).

5 Otrokov, M. M. *et al.* Unique Thickness-Dependent Properties of the van der Waals Interlayer Antiferromagnet $MnBi_2Te_4$ Films. *Phys. Rev. Lett.* **122**, 107202 (2019).

6 Otrokov, M. M. *et al.* Prediction and observation of an antiferromagnetic topological insulator. *Nature* **576**, 416-422 (2019).

7 Liu, C. *et al.* Robust axion insulator and Chern insulator phases in a two-dimensional antiferromagnetic topological insulator. *Nat. Mater.* **19**, 522-527 (2020).

8 Gong, Y. *et al.* Experimental realization of an intrinsic magnetic topological insulator. *Chin. Phys. Lett.* **36**, 076801 (2019).

9 Thomson, R., Leburn, C. & Reid, D. *Ultrafast Nonlinear Optics*. (Springer, 2013).

10 Kwiat, P. G., Waks, E., White, A. G., Appelbaum, I. & Eberhard, P. H. Ultrabright source of polarization-entangled photons. *Phys. Rev. A* **60**, R773-R776 (1999).

11 Gisin, N., Ribordy, G., Tittel, W. & Zbinden, H. Quantum cryptography. *Rev. Mod. Phys.* **74**, 145-195 (2002).

12 Zhao, M. *et al.* Atomically phase-matched second-harmonic generation in a 2D crystal. *Light Sci. Appl.* **5**, e16131 (2016).

13 Wang, H. & Qian, X. Giant Optical Second Harmonic Generation in Two-Dimensional Multiferroics. *Nano Lett.* **17**, 5027-5034 (2017).

14 Sipe, J. & Shkrebtii, A. Second-order optical response in semiconductors. *Phys. Rev. B* **61**, 5337 (2000).

15 Young, S. M. & Rappe, A. M. First Principles Calculation of the Shift Current Photovoltaic Effect in Ferroelectrics. *Phys. Rev. Lett.* **109**, 116601 (2012).

16 Rangel, T. *et al.* Large Bulk Photovoltaic Effect and Spontaneous Polarization of Single-Layer Monochalcogenides. *Phys. Rev. Lett.* **119**, 067402 (2017).

17 Wang, H. & Qian, X. Ferroicity-driven nonlinear photocurrent switching in time-reversal invariant ferroic materials. *Sci. Adv.* **5**, eaav9743 (2019).

18 von Baltz, R. & Kraut, W. Theory of the bulk photovoltaic effect in pure crystals. *Phys. Rev. B* **23**, 5590-5596 (1981).

19 Nastos, F. & Sipe, J. Optical rectification and current injection in unbiased semiconductors. *Phys. Rev. B* **82**, 235204 (2010).

20 Panday, S. R., Barraza-Lopez, S., Rangel, T. & Fregoso, B. M. Injection current in ferroelectric group-IV monochalcogenide monolayers. *Phys. Rev. B* **100**, 195305 (2019).

21 de Juan, F., Grushin, A. G., Morimoto, T. & Moore, J. E. Quantized circular photogalvanic effect in Weyl semimetals. *Nat. Commun.* **8**, 15995 (2017).

22 Sodemann, I. & Fu, L. Quantum Nonlinear Hall Effect Induced by Berry Curvature Dipole in Time-Reversal Invariant Materials. *Phys. Rev. Lett.* **115**, 216806 (2015).

23 Moore, J. E. & Orenstein, J. Confinement-Induced Berry Phase and Helicity-Dependent Photocurrents. *Phys. Rev. Lett.* **105**, 026805 (2010).

24 Wang, H. & Qian, X. Ferroelectric nonlinear anomalous Hall effect in few-layer WTe_2. *npj Computational Materials* **5**, 119 (2019).

25 Shi, L.-k., Zhang, D., Chang, K. & Song, J. C. Geometric photon-drag effect and nonlinear shift current in centrosymmetric crystals. *Preprint at arXiv:2006.08358* (2020).

26 Xiao, J. *et al.* Berry curvature memory through electrically driven stacking transitions. *Nat. Phys.* **16**, 1028–1034 (2020).

27 Fregoso, B. M. Bulk photovoltaic effects in the presence of a static electric field. *Phys. Rev. B* **100**, 064301 (2019).

28 Zhang, Y. *et al.* Switchable magnetic bulk photovoltaic effect in the two-dimensional magnet CrI_3. *Nat. Commun.* **10**, 3783 (2019).

29 de Juan, F. *et al.* Difference frequency generation in topological semimetals. *Phys. Rev. Research* **2**, 012017 (2020).

30 Fei, R., Song, W. & Yang, L. Giant photogalvanic effect and second-harmonic generation in magnetic axion insulators. *Phys. Rev. B* **102**, 035440 (2020).

31 Bhalla, P., MacDonald, A. H. & Culcer, D. Resonant Photovoltaic Effect in Doped Magnetic Semiconductors. *Phys. Rev. Lett.* **124**, 087402 (2020).

32 Birss, R. R. *Symmetry and Magnetism*. Vol. 863 (North-Holland Amsterdam, 1964).

33 Hohenberg, P. & Kohn, W. Inhomogeneous electron gas. *Phys. Rev. B* **136**, B864-B871 (1964).

34 Kohn, W. & Sham, L. J. Self-consistent equations including exchange and correlation effects. *Phys. Rev.* **140**, A1133-A1138 (1965).

35 Kresse, G. & Furthmüller, J. Efficient iterative schemes for *ab initio* total-energy calculations using a plane-wave basis set. *Phys. Rev. B* **54**, 11169-11186 (1996).

36 Kresse, G. & Furthmüller, J. Efficiency of ab-initio total energy calculations for metals and semiconductors using a plane-wave basis set. *Comput. Mater. Sci.* **6**, 15-50 (1996).

37 Blöchl, P. E. Projector augmented-wave method. *Phys. Rev. B* **50**, 17953-17979 (1994).

38 Marzari, N., Mostofi, A. A., Yates, J. R., Souza, I. & Vanderbilt, D. Maximally localized Wannier functions: Theory and applications. *Rev. Mod. Phys.* **84**, 1419-1475 (2012).

39 Qian, X. *et al.* Quasiatomic orbitals for *ab initio* tight-binding analysis. *Phys. Rev. B* **78**, 245112 (2008).

40 Mostofi, A. A. *et al.* An updated version of wannier90: A tool for obtaining maximally-localised Wannier functions. *Comput. Phys. Commun.* **185**, 2309-2310 (2014).

41 Du, S. *et al.* Berry curvature engineering by gating two-dimensional antiferromagnets. *Phys. Rev. Research* **2**, 022025 (2020).

42 Morimoto, T. & Nagaosa, N. Nonreciprocal current from electron interactions in noncentrosymmetric crystals: roles of time reversal symmetry and dissipation. *Sci. Rep.* **8**, 2973 (2018).

43 Lee, J. M., Kottos, T. & Shapiro, B. Macroscopic magnetic structures with balanced gain and loss. *Phys. Rev. B* **91**, 094416 (2015).

44 Perdew, J. P., Burke, K. & Ernzerhof, M. Generalized gradient approximation made simple. *Phys. Rev. Lett.* **77**, 3865-3868 (1996).

45 Grimme, S., Antony, J., Ehrlich, S. & Krieg, H. A consistent and accurate ab initio parametrization of density functional dispersion correction (DFT-D) for the 94 elements H-Pu. *J. Chem. Phys.* **132**, 154104 (2010).

Figure Legends

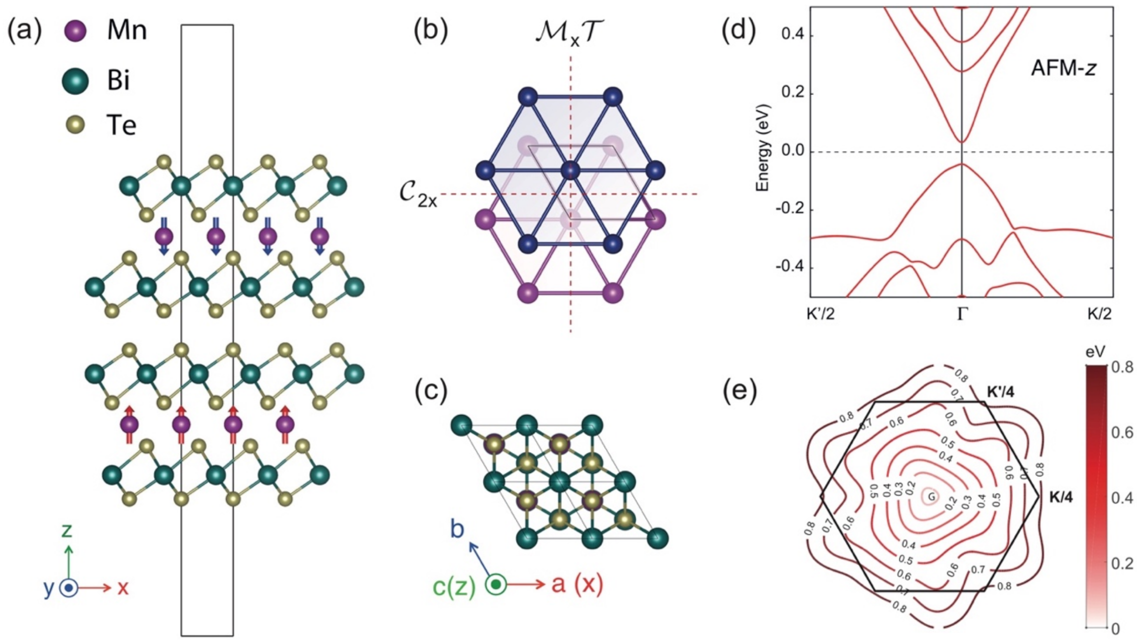

Fig. 1 Crystal structure and electronic structure of bilayer AFM-*z* $MnBi_2Te_4$. a-c The side and top view of bilayer AFM-*z* $MnBi_2Te_4$. **b** Selected magnetic symmetry elements in bilayer AFM-*z* $MnBi_2Te_4$ with the corresponding point group of $\overline{3}'m'$ in international notation or $D_{3d}(D_3)$ in Schoenflies notation. Two magnetic symmetry elements are illustrated in the plot, including two-fold rotation symmetry around *x*-axis $C_{2x} = \mathcal{M}_y\mathcal{M}_z$, and the combination of mirror symmetry and time-reversal symmetry $\mathcal{M}_x\mathcal{T}$. **d** Electronic band structure of bilayer AFM-*z* $MnBi_2Te_4$ near the Fermi level. **e** Contour plot of the energy difference between bottom conduction band and top valence band.

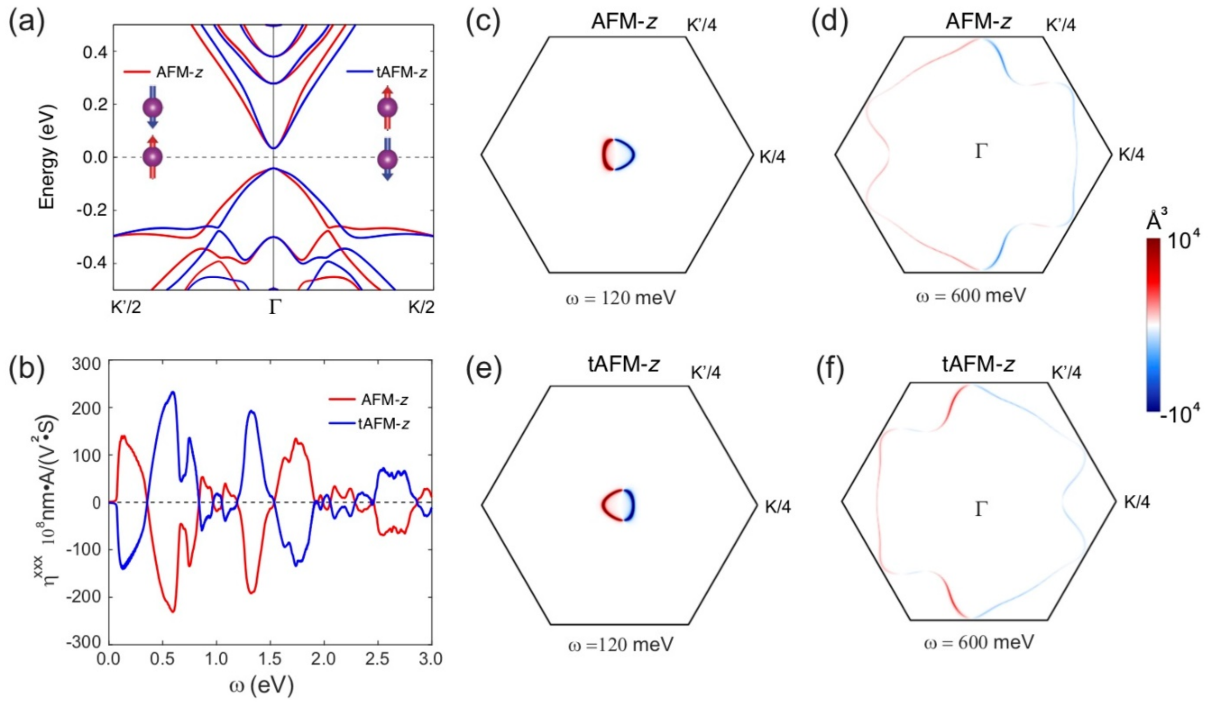

Fig. 2 Magnetic injection current (MIC) in bilayer $MnBi_2Te_4$ with magnetic ordering in AFM-*z* (↑↓) and time-reversed AFM-*z* (tAFM, ↓↑). a Band structure of bilayer AFM-*z* and tAFM-*z* $MnBi_2Te_4$ with spin-orbit coupling taken into account. **b** Frequency-dependent magnetic injection current response of bilayer AFM-*z* and tAFM-*z* $MnBi_2Te_4$. **c-f** Microscopic distribution of MIC $f_{mn}\Delta_{mn}^{a}\{r_{nm}^{b}, r_{mn}^{c}\}\delta(\omega_{nm} - \omega)$ between top valence band and bottom conduction band at different frequencies of 120 meV and 600 meV in bilayer AFM-*z* and tAFM-*z* $MnBi_2Te_4$. It shows that MIC can be switched between two time-reversed magnetic orders AFM-*z* (↑↓) and tAFM (↓↑).

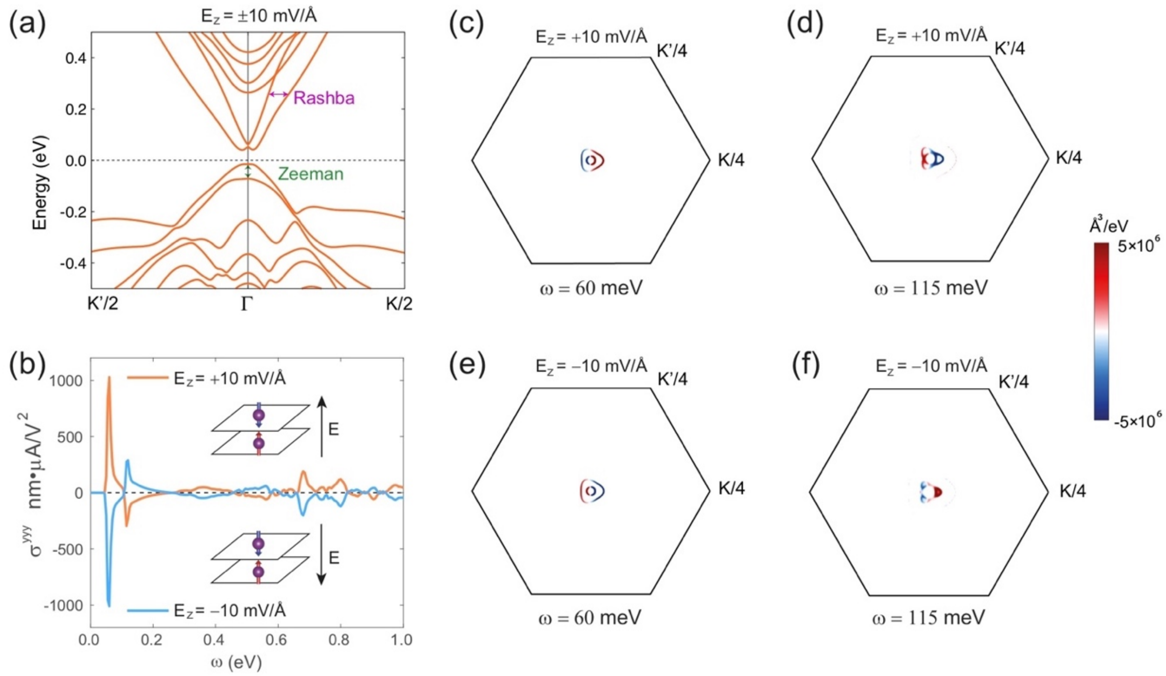

Fig. 3 Normal shift current (NSC) in bilayer $MnBi_2Te_4$ with magnetic ordering AFM-*z* (↑↓) under external electric field $\boldsymbol{E_z = 10}$ mV $\cdot$ Å^{-1}. **a** Band structure of bilayer AFM-*z* under external electric field $E_z = 10$ mV $\cdot$ Å^{-1}. (b), Frequency-dependent NSC response of bilayer AFM-*z* $MnBi_2Te_4$ under external electric field $E_z = \pm 10$ mV $\cdot$ Å^{-1}. **c-f** Microscopic distribution of NSC $\sum_{mn\sigma} f_{nm}\left(r^b_{mn} r^c_{nm;k^a} + r^c_{mn} r^b_{nm;k^a}\right)\left(\delta(\omega_{nm} - \omega) + \delta(\omega_{mn} - \omega)\right)$ at different frequencies in bilayer AFM-*z* external electric field $E_z = \pm 10$ mV $\cdot$ Å^{-1}. It demonstrates that NSC can be switched by applying electric field along +*z*/-*z* out-of-plane directions.

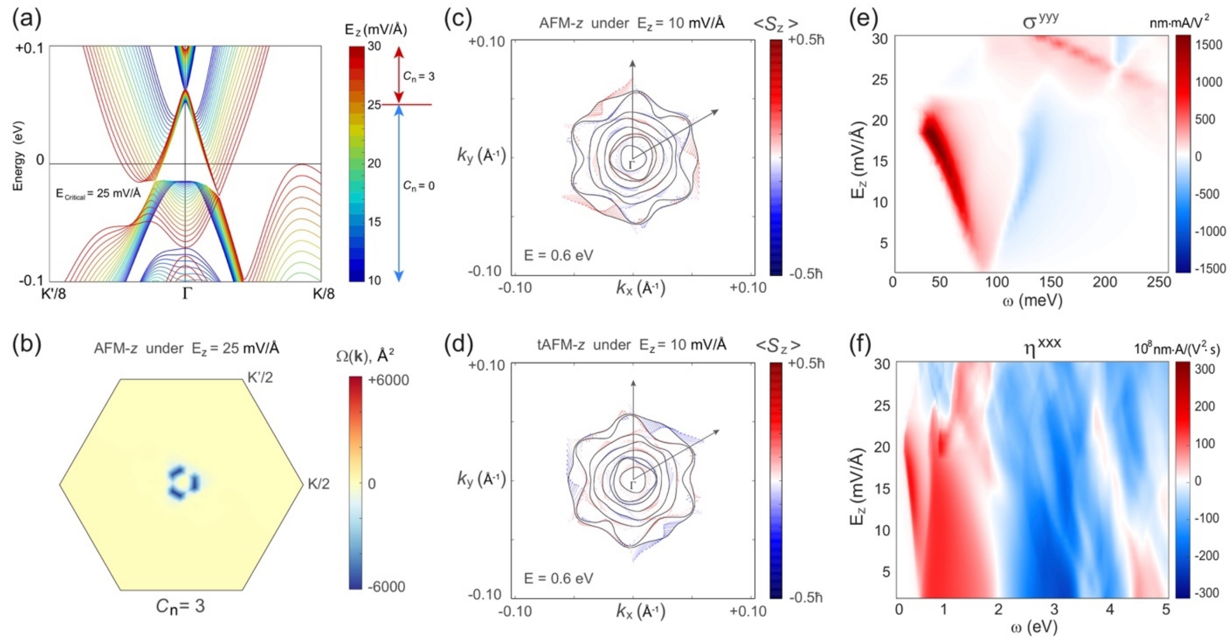

Fig. 4 Electric field dependent electric structure, topology, and photocurrent responses in bilayer AFM-*z* $MnBi_2Te_4$. **a** Electric field dependent band structure. **b** Berry curvature at the critical vertical electric field of $E_z = 25\ \mathrm{mV} \cdot \text{Å}^{-1}$ where it undergoes topological phase transition from zero-plateau quantum anomalous Hall insulator with Chern number $C_n = 0$ to high Chern number quantum anomalous Hall insulator ($C_n = 3$). **c-d** Spin polarization of bilayer $MnBi_2Te_4$ at energy of 0.6 eV with AFM-*z* and tAFM-*z* magnetic ordering under a vertical electric field of $E_z = 10\ \mathrm{mV} \cdot \text{Å}^{-1}$ which enables large spin splitting. **e** Normal shift photocurrent (NSC) susceptibility, $\sigma_{\mathrm{NSC}}^{yyy}$, in bilayer AFM-*z* $MnBi_2Te_4$ under varying external static vertical electric field E_z and fundamental frequency ω. **f** Magnetic injection current (MIC) susceptibility, $\eta_{\mathrm{MIC}}^{xxx}$, in bilayer AFM-*z* $MnBi_2Te_4$ under varying external static vertical electric field E_z and fundamental frequency ω.

Supplementary Information

Electrically and magnetically switchable nonlinear photocurrent in $\mathcal{PT}$-symmetric magnetic topological quantum materials

Hua Wang[1] and Xiaofeng Qian[1]*

[1]*Department of Materials Science and Engineering, Texas A&M University, College Station, Texas 77843, USA*

* Corresponding author: feng@tamu.edu

Supplementary Note 1

Derivation of nonlinear photocurrent responses using density matrix formalism. We start with many-body Hamiltonian including spin-orbit coupling (SOC)

$$H_0 = \int d\mathbf{r}\Psi^{\dagger}\mathcal{H}_0\Psi + H_{\text{rest}} \tag{1}$$

where

$$\mathcal{H}_0 = \frac{\boldsymbol{p}^2}{2m} + V(\boldsymbol{r}) + \frac{e\hbar}{4m^2c^2}[\nabla V(\boldsymbol{r}) \times \boldsymbol{p}] \cdot \boldsymbol{\sigma} \tag{2}$$

is the ground state Hamiltonian density, Ψ is the field operator, and $\boldsymbol{\sigma}$ is the Pauli matrix which is contracted in the band index for the sake of simplicity. H_{rest} contains the remaining many-body interactions, e.g., electron-phonon interaction. The interacting Hamiltonian density under electric field $\mathbf{E}(t) = \boldsymbol{E}e^{i\omega t}$ in length gauge is given by

$$\mathcal{H}_{\text{int}} = \mathcal{H}_0 - e\mathbf{r} \cdot \mathbf{E}(t). \tag{3}$$

We obtain the interacting Hamiltonian in the second quantization formalism

$$H_{\text{int}}(t) = \sum_n \int d\mathbf{k}\hbar\omega_n a_n^{\dagger} a_n - e\mathbf{E}(t) \cdot \sum_{n,m} \int d\mathbf{k}\, \mathbf{r}_{nm} a_n^{\dagger} a_m + H_{\text{rest}}. \tag{4}$$

Here, $\mathbf{r}_{nm} = \langle n\mathbf{k}|\mathbf{r}|m\mathbf{k}\rangle$ is the dipole matrix element including intraband and interband part. The intraband current can be written as

$$\boldsymbol{J} = \frac{e}{\mathcal{V}}\sum_{nm} \int d\mathbf{k} \left[\mathbf{v}_{nm}\delta_{nm} - \frac{e}{\hbar}(\mathbf{E} \times \boldsymbol{\Omega}_n)\delta_{nm} - \frac{e}{\hbar}\mathbf{E} \cdot \mathbf{r}_{nm;\mathbf{k}}\right] a_n^{\dagger} a_m. \tag{5}$$

The second term is related to anomalous velocity induced by Berry curvature $\boldsymbol{\Omega}_n$ and the third term is related to the shift current. The density matrix operator ρ obeys the von Neumann equation

$$i\hbar\frac{d\rho(t)}{dt} = [H(t), \rho(t)]. \tag{6}$$

The matrix elements are given by

$$\begin{aligned}\left\langle n\mathbf{k}\left|i\hbar\frac{d\rho(t)}{dt}\right|m\mathbf{k}\right\rangle &= i\hbar\frac{d\rho_{nm}(t)}{dt} = \langle n\mathbf{k}|[H_0 - e\mathbf{r} \cdot \mathbf{E}]|m\mathbf{k}\rangle \\ &= \hbar\omega_{nm}\rho_{nm} - e\mathbf{E}(t)\left[i\rho_{nm;\mathbf{k}} + \left(\sum_l \mathbf{r}_{nl}\rho_{lm} - \sum_l \rho_{nl}\mathbf{r}_{lm}\right)\right],\end{aligned} \tag{7}$$

we thus obtain the equation for density matrix elements

$$\frac{d\rho_{nm}(t)}{dt} = -i\omega_{nm}\rho_{nm} - \frac{e}{\hbar}\mathbf{E}(t)\left[\rho_{nm;\mathbf{k}} - i\left(\sum_l \mathbf{r}_{nl}\rho_{lm} - \sum_l \rho_{nl}\mathbf{r}_{lm}\right)\right]. \tag{8}$$

This equation can be solved recursively

$$\begin{cases} \dfrac{d\rho_{nm}^{(0)}}{dt} = -i\omega_{nm}\rho_{nm}^{(0)} \\ \dfrac{d\rho_{nm}^{(1)}}{dt} = -i\omega_{nm}\rho_{nm}^{(1)} - \dfrac{e}{\hbar}\mathbf{E}(t)\left[\rho_{nm;\mathbf{k}}^{(0)} - i\left(\sum_l \mathbf{r}_{nl}\rho_{lm}^{(0)} - \sum_l \rho_{nl}^{(0)}\mathbf{r}_{lm}\right)\right] \\ \vdots \\ \dfrac{d\rho_{nm}^{(N)}}{dt} = -i\omega_{nm}\rho_{nm}^{(N)} - \dfrac{e}{\hbar}\mathbf{E}(t)\left[\rho_{nm;\mathbf{k}}^{(N-1)} - i\left(\sum_l \mathbf{r}_{nl}\rho_{lm}^{(N-1)} - \sum_l \rho_{nl}^{(N-1)}\mathbf{r}_{lm}\right)\right] \end{cases} \tag{9}$$

Let's start with the ground state density matrix $\rho_{nm}^{(0)} = f_n\delta_{nm}$. The anomalous Hall current can be recovered from the second term in the current expression

$$\boldsymbol{J}_{\text{ahc}} = -\frac{e^2}{\hbar}\mathbf{E} \times \int d\mathbf{k} \sum_n f_n\Omega_n(\mathbf{k}). \tag{10}$$

We then obtain the first order perturbative intraband and interband density matrix with electric field $E^b(t) = \sum_\beta E_\beta^b e^{-i\omega_\beta t}$

$$\rho_{\text{intra},nn}^{(1)} = \rho_{i,nn}^{(1)} = -\frac{e}{\hbar}\sum_{b\beta}\frac{i}{\omega_\beta}\partial_b f_n E_\beta^b e^{i\omega_\beta t} \tag{11}$$

$$\rho_{\text{inter},nm}^{(1)} = \rho_{e,nm}^{(1)} = \frac{e}{\hbar}\sum_{b\beta}\frac{r_{nm}^b f_{mn}}{\omega_{nm} - \omega_\beta}E_\beta^b e^{i\omega_\beta t} \tag{12}$$

The shift current response is

$$\begin{aligned} J_{\text{SC}}^a &= -\frac{e^2}{\hbar}\int d\mathbf{k}\sum_{nm}\mathbf{E}\cdot\mathbf{r}_{nm;k^a}\,\rho_{\text{inter},mn}^{(1)} \\ &= -\frac{e^3}{\hbar^2}\int d\mathbf{k}\sum_{nmbc\beta\gamma}\frac{r_{nm;k^a}^c r_{mn}^b f_{nm}}{\omega_{mn} - \omega_\beta}E_\gamma^c E_\beta^b\, e^{-i(\omega_\beta+\omega_\gamma)t}. \end{aligned} \tag{13}$$

The above expression can be symmetrized by exchanging the indices $b\beta \leftrightarrow c\gamma$ and setting $\omega_\beta + \omega_\gamma = 0$. We then obtain

$$J_{\text{SC}}^a = -\frac{i\pi e^3}{2\hbar^2}\int d\mathbf{k}\sum_{mn} f_{nm}\left(r_{mn}^b r_{nm;k^a}^c - r_{nm}^c r_{mn;k^a}^b\right)\delta\left(\omega_{nm} - \omega_\beta\right)E^b\left(\omega_\beta\right)E^c\left(-\omega_\beta\right). \tag{14}$$

The Sokhotski-Plemelj formula is used in the integral with a relaxation time η

$$\frac{1}{\omega_{mn} - \omega - i\eta} = \wp\frac{1}{\omega_{mn} - \omega} + i\pi\delta(\omega_{mn} - \omega). \tag{15}$$

By substituting the first order density matrix into the previous recursive equations, we get the second order density matrix

$$\rho_{ii,nn}^{(1)} = -\frac{e}{\hbar}\sum_a \frac{i}{\omega_\alpha}\partial_a\rho_{i,nn}^{(1)}E_\alpha^a e^{-i\omega_\alpha t} = -\frac{e^2}{\hbar^2}\sum_{ab\alpha\beta}\frac{1}{\omega_\alpha\omega_\beta}\partial_a\partial_b f_n E_\alpha^a E_\beta^b e^{-i(\omega_\alpha+\omega_\beta)t} \tag{16}$$

$$\rho_{ie,nm}^{(2)} = \frac{e}{\hbar(\omega_\alpha+\omega_\beta)}\sum_l E_\alpha^a(r_{nl}^a\rho_{e,lm}^{(1)} - \rho_{e,nl}^{(1)}r_{ln}^a)$$
$$= \frac{e^2}{\hbar^2(\omega_\alpha+\omega_\beta)}\sum_{abl\alpha\beta} r_{nl}^a r_{ln}^b f_{nl}\left(\frac{1}{\omega_{ln}-\omega_\beta}+\frac{1}{\omega_{nl}-\omega_\beta}\right)E_\alpha^a E_\beta^b e^{-i(\omega_\alpha+\omega_\beta)t}. \tag{17}$$

$\rho_{ii,nn}^{(1)}$ can contribute to the anomalous current related to the second order derivative of the occupation number. Using integration by parts, we obtain a new third order intraband current determined by Berry curvature quadrupole in time-reversal breaking metallic systems. We named it Berry quadrupole current which is given by

$$J_{\mathrm{BQC}}^e = \frac{e^4}{\hbar^3}\int d\mathbf{k}\sum_{abcdn\alpha\beta}\epsilon_{ecd}\Omega_n^d\frac{1}{\omega_\alpha\omega_\beta}\partial_a\partial_b f_n E_\alpha^a E_\beta^b E_\gamma^c e^{-i(\omega_\alpha+\omega_\beta+\omega_\gamma)t}. \tag{18}$$

A direct current can be generated under static electric field $\omega_\gamma = 0$ and optical field $\omega_\alpha = -\omega_\beta = \omega$. The injection current can be derived from $\rho_{ie,nm}^{(2)}$. We have

$$\frac{dJ_{\mathrm{IC}}^a}{dt} = -\frac{ie^3}{\hbar^2}\int d\mathbf{k}\sum_{bcmn} f_{mn}\Delta_{nm}^a r_{nm}^b r_{mn}^c\frac{1}{\omega_{nm}-\omega_\beta}E_\alpha^b E_\beta^c e^{-i(\omega_\alpha+\omega_\beta)t} \tag{19}$$

By setting $\omega_\alpha+\omega_\beta = 0$ and using the Sokhotski-Plemelj formula, we obtain the injection current

$$\frac{dJ_{\mathrm{IC}}^a}{dt} = -\frac{\pi e^3}{\hbar^2}\int d\mathbf{k}\sum_{bcmn} f_{mn}\Delta_{mn}^a r_{nm}^b r_{mn}^c\,\delta(\omega_{nm}-\omega_\beta)E^b(\omega_\beta)E^c(-\omega_\beta). \tag{20}$$

Next we move to the derivation of the magnetic shift photocurrent (MSC) by taking out the summation with $\mathrm{Im}(E^b E^{c^*})$

$$
\begin{aligned}
\sum_{mn\mathbf{k}\sigma} f_{nm}\left(r^b_{mn}r^c_{nm;k^a} - r^c_{nm}r^b_{mn;k^a}\right)\delta(\omega_{nm}-\omega) \\
&- \sum_{mn\mathbf{k}\sigma} f_{mn}\left(r^b_{nm}r^c_{mn;k^a} - r^c_{mn}r^b_{nm;k^a}\right)\delta(\omega_{nm}-\omega) \\
&= \sum_{mn\mathbf{k}\sigma} f_{nm}\left(r^b_{mn}r^c_{nm;k^a} - r^c_{nm}r^b_{mn;k^a}\right)\delta(\omega_{nm}-\omega) \\
&- \sum_{mn\mathbf{k}\sigma} f_{nm}\left(r^c_{nm}r^b_{mn;k^a} - r^b_{nm}r^c_{mn;k^a}\right)\delta(\omega_{nm}-\omega) \\
&= \sum_{mn\mathbf{k}\sigma} f_{nm}\left(r^b_{mn}r^c_{nm;k^a} - r^c_{nm}r^b_{mn;k^a}\right)\delta(\omega_{nm}-\omega) \\
&- \sum_{mn\mathbf{k}\sigma} f_{mn}\left(r^c_{mn}r^b_{nm;k^a} - r^b_{mn}r^c_{nm;k^a}\right)\delta(\omega_{mn}-\omega) \\
&= \sum_{mn\mathbf{k}\sigma} f_{nm}\left(r^b_{mn}r^c_{nm;k^a} - r^c_{nm}r^b_{mn;k^a}\right)\delta(\omega_{nm}-\omega) \\
&- \sum_{mn\mathbf{k}\sigma} f_{nm}\left(r^b_{mn}r^c_{nm;k^a} - r^c_{mn}r^b_{nm;k^a}\right)\delta(\omega_{mn}-\omega) \\
&= \sum_{mn\mathbf{k}\sigma} f_{nm}\left(r^b_{mn}r^c_{nm;k^a} - r^c_{nm}r^b_{mn;k^a}\right)\left(\delta(\omega_{nm}-\omega) - \delta(\omega_{mn}-\omega)\right).
\end{aligned}
\tag{21}
$$

Hence, MSC conductivity can be written as

$$
\sigma^{abc}_{\mathrm{MSC}} = -\frac{i\pi e^3}{4\hbar^2}\int[d\mathbf{k}]\sum_{mn\sigma} f_{nm}\left(r^b_{mn}r^c_{nm;k^a} - r^c_{mn}r^b_{nm;k^a}\right)\left(\delta(\omega_{nm}-\omega) - \delta(\omega_{mn}-\omega)\right). \tag{22}
$$

For normal shift current (NSC),

$$
\sigma^{abc}_{\mathrm{NSC}} = -\frac{i\pi e^3}{4\hbar^2}\int[d\mathbf{k}]\sum_{mn\sigma} f_{nm}\left(r^b_{mn}r^c_{nm;k^a} + r^c_{mn}r^b_{nm;k^a}\right)\left(\delta(\omega_{nm}-\omega) + \delta(\omega_{mn}-\omega)\right). \tag{23}
$$

In addition, we have $r^c_{nm}(\mathbf{k}) = |r^c_{nm}(\mathbf{k})|e^{i\phi^c_{nm}(\mathbf{k})}$, hence

$$
\begin{aligned}
r^b_{mn}r^c_{nm;k^a} &= r^b_{mn}\left(\frac{\partial r^c_{nm}}{\partial k^a} - ir^c_{nm}(\mathcal{A}^a_m - \mathcal{A}^a_n)\right) \\
&= r^b_{mn}\left(\frac{\partial|r^c_{nm}|}{\partial k^a}e^{i\phi^c_{nm}} + ir^c_{nm}\frac{\partial\phi^c_{nm}}{\partial k^a} - ir^c_{nm}(\mathcal{A}^a_m - \mathcal{A}^a_n)\right) \\
&= \left(r^b_{mn}\frac{\partial|r^c_{nm}|}{\partial k^a}e^{i\phi^c_{nm}} + ir^b_{mn}r^c_{nm}\left(\frac{\partial\phi^c_{nm}}{\partial k^a} - (\mathcal{A}^a_m - \mathcal{A}^a_n)\right)\right)
\end{aligned}
\tag{24}
$$

$$
r^c_{mn}r^b_{nm;k^a} = \left(r^c_{mn}\frac{\partial|r^b_{nm}|}{\partial k^a}e^{i\phi^b_{nm}} + ir^c_{mn}r^b_{nm}\left(\frac{\partial\phi^b_{nm}}{\partial k^a} - (\mathcal{A}^a_m - \mathcal{A}^a_n)\right)\right) \tag{25}
$$

For nonzero optical dipole matrix $\left|r^b_{nm}\right| \neq 0$, we have

$$
r^b_{mn}\frac{\partial|r^c_{nm}|}{\partial k^a}e^{i\phi^c_{nm}} = \frac{r^b_{mn}r^c_{nm}}{|r^c_{nm}|}\frac{\partial|r^c_{nm}|}{\partial k^a} = r^b_{mn}r^c_{nm}\frac{\partial\ln|r^c_{nm}|}{\partial k^a}. \tag{26}
$$

Under time-reversal symmetry, the integral of the real part contributing to MSC of the above term is zero and the imaginary part of $r_{mn}^{b}r_{nm}^{c}$ contributing to NSC is vanishing when $b = c$. The shift vector is real, we thus only take the real part of $r_{mn}^{b}r_{nm}^{c}R_{mn}^{a}$ to obtain the NSC conductivity

$$\mathrm{Re}\left(r_{mn}^{b}r_{nm}^{c}\right) = \frac{1}{2}\left(r_{mn}^{b}r_{nm}^{c} + r_{mn}^{c}r_{nm}^{b}\right) \tag{27}$$

$$\sigma_{\mathrm{NSC}}^{abc} = -\frac{\pi e^3}{4\hbar^2}\int [d\mathbf{k}] \sum_{mn\boldsymbol{\sigma}} f_{nm}\left(R_{mn}^{a,b}(\mathbf{k}) + R_{mn}^{a,c}(\mathbf{k})\right)\{r_{nm}^{b}, r_{mn}^{c}\}\delta(\omega_{nm} - \omega). \tag{28}$$

There is an additional term $\Omega_{mn}^{d}\frac{\partial \ln|r_{nm}^{c}|}{\partial k^a}$ which will contribute to NSC for circularly polarized light in time-reversal breaking systems. Similarly, we take the imaginary part of $r_{mn}^{b}r_{nm}^{c}$ to obtain the MSC conductivity. We have

$$\left(r_{mn}^{b}r_{nm}^{c}\right)^* = \left(r_{mn}^{c}r_{nm}^{b}\right) \tag{29}$$

$$\mathrm{Im}\left(r_{mn}^{b}r_{nm}^{c}\right)R_{mn}^{a,b}(\mathbf{k}) - \mathrm{Im}\left(r_{mn}^{c}r_{nm}^{b}\right)R_{mn}^{a,c}(\mathbf{k}) = \mathrm{Im}\left(r_{mn}^{b}r_{nm}^{c}\right)\left(R_{mn}^{a,b}(\mathbf{k}) + R_{mn}^{a,c}(\mathbf{k})\right) \tag{30}$$

$$\mathrm{Im}\left(r_{mn}^{b}r_{nm}^{c}\right) = \frac{1}{2i}\left(r_{mn}^{b}r_{nm}^{c} - r_{mn}^{c}r_{nm}^{b}\right) \tag{31}$$

Finally, we obtain the compact form

$$\sigma_{\mathrm{MSC}}^{abc} = -\frac{\pi e^3}{4i\hbar^2}\int [d\mathbf{k}] \sum_{mn\boldsymbol{\sigma}} f_{nm}\left(R_{mn}^{a,b}(\mathbf{k}) + R_{mn}^{a,c}(\mathbf{k})\right)\Omega_{mn}^{d}(\mathbf{k})\delta(\omega_{nm} - \omega). \tag{32}$$

Supplementary Note 2

Group theoretical analysis of bilayer $MnBi_2Te_4$ with different magnetic orderings.

1) Magnetic point group of bilayer AFM-*z* $MnBi_2Te_4$ is:

$$\bar{3}'m' = D_{3d}(D_3) = D_3 \oplus (D_{3d} - D_3)\mathcal{T} = \{E, 2C_3, 3C_2', i\mathcal{T}, 2S_6\mathcal{T}, 3\sigma_d\mathcal{T}\}. \tag{31}$$

2) Magnetic point group of bilayer FM-*z* $MnBi_2Te_4$ is:

$$\bar{3}m' = D_{3d}(C_{3i}) = C_{3i} \oplus (D_{3d} - C_{3i})\mathcal{T} = \{E, C_3, C_3^2, i, S_6^5, S_6, 3C_2'\mathcal{T}, 3\sigma_d\mathcal{T}\}. \tag{31}$$

3) Magnetic point group of bilayer AFM-*x* $MnBi_2Te_4$ is:

$$2'/m = C_{2h}(C_s) = C_s \oplus (C_{2h} - C_s)\mathcal{T} = \{E, \sigma_x, C_{2x}\mathcal{T}, i\mathcal{T}\}. \tag{31}$$

Magnetization along x-axis breaks the three-fold rotation symmetry and transform the crystal to monoclinic phase C_{2h}. It is $\mathcal{PT}$-symmetric with nonvanishing MIC.

4) Magnetic point group of bilayer FM-*x* $MnBi_2Te_4$ is:

$$2/m = \{E, i, C_{2x}, \sigma_x\} \tag{31}$$

which is identical to the geometric point group C_{2h}.

Supplementary Tables

D_{3d}	E	$2C_3(z)$	$3C_2'$	i	$2S_6$	$3\sigma_d$	Basis function
A_{1g}	+1	+1	+1	+1	+1	+1	
A_{2g}	+1	+1	-1	+1	+1	-1	R_z
E_g	+2	-1	0	+2	-1	0	(R_x, R_y)
A_{1u}	+1	+1	+1	-1	-1	-1	
A_{2u}	+1	+1	-1	-1	-1	+1	z
E_u	+2	-1	0	-2	+1	0	(x, y)

Table S1 Character table for D_{3d}

operator / tensor	Even rank tensor			Odd rank tensor		
	$\mathcal{T}$	$\mathcal{P}$	$\mathcal{PT}$	$\mathcal{T}$	$\mathcal{P}$	$\mathcal{PT}$
Polar *i*-tensor	+1	+1	+1	+1	-1	-1
Polar *c*-tensor	-1	+1	-1	-1	-1	+1
Axial *i*-tensor	+1	-1	-1	+1	+1	+1
Axial *c*-tensor	-1	-1	+1	-1	+1	-1

Table S2 Transformation of polar/axial *i*-/*c*-tensors under space inversion $\mathcal{P}$, time reversal operation $\mathcal{T}$, and $\mathcal{PT}$

Magnetic ordering	Symmetry operations			Magnetic point group
AFM-*z*	$\mathcal{PT}$	$\mathcal{M}_x\mathcal{T}$	$C_{2x} = \mathcal{M}_y\mathcal{M}_z$	$\bar{3}'m'$ or $D_{3d}(D_3)$
AFM-*x*	$\mathcal{PT}$	$\mathcal{M}_x$	$C_{2x}\mathcal{T} = \mathcal{M}_y\mathcal{M}_z\mathcal{T}$	$2'/m$ or $C_{2h}(C_s)$
FM-*z*	$\mathcal{P}$	$\mathcal{M}_x\mathcal{T}$	$C_{2x}\mathcal{T}$	$\bar{3}m'$ or $D_{3d}(C_{3i})$
FM-*x*	$\mathcal{P}$	$\mathcal{M}_x$	C_{2x}	$2/m$ or C_{2h}

Table S3 Selected symmetry operations and magnetic point group in bilayer $MnBi_2Te_4$ with different magnetic ordering

Supplementary Figures

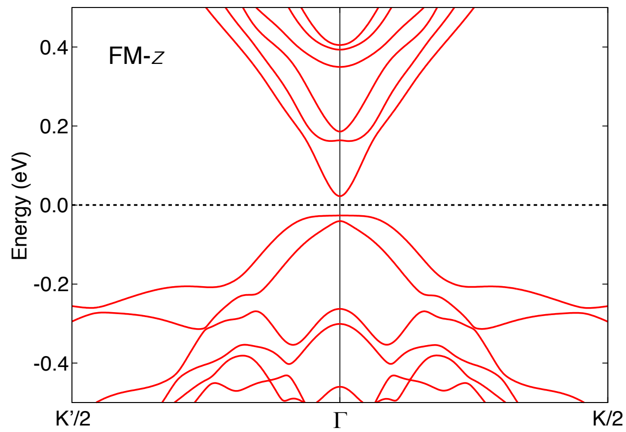

Figure S1 Band structure of bilayer $MnBi_2Te_4$ with FM-*z* magnetic ordering. Each band is symmetric with respect to $\pm\boldsymbol{k}$ points, hence magnetic injection current vanishes.

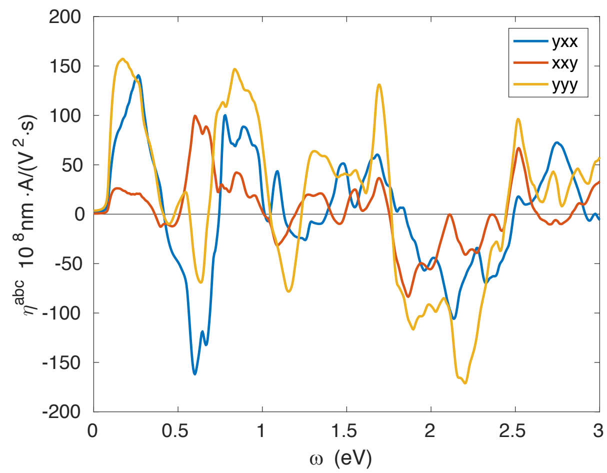

Figure S2 Magnetic injection current (MIC) in bilayer $MnBi_2Te_4$ with AFM-*x* magnetic ordering. bilayer AFM-*x* $MnBi_2Te_4$ preserves $\mathcal{PT}$-symmetry, thus allows for nonvanishing MIC susceptibility $\eta_{\mathrm{MIC}}^{xxy}$, $\eta_{\mathrm{MIC}}^{yxx}$, and $\eta_{\mathrm{MIC}}^{yyy}$.

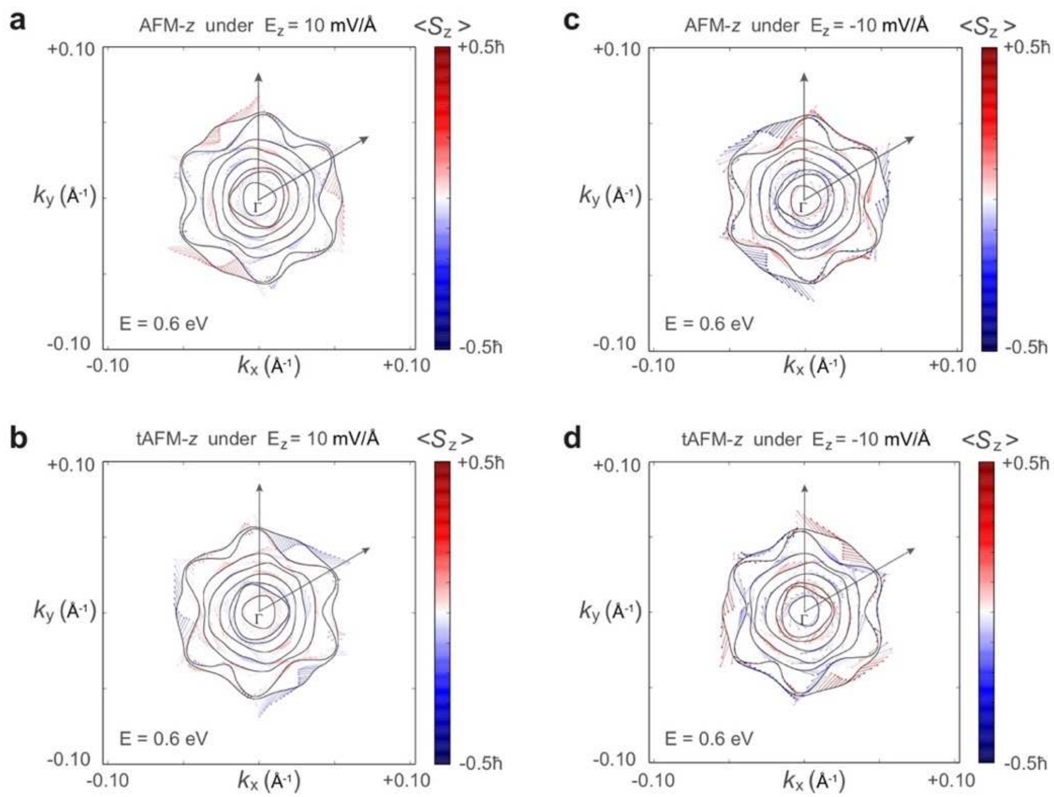

Figure S3 Spin polarization of bilayer $MnBi_2Te_4$ at energy of 0.6 eV with AFM-*z* and tAFM-*z* magnetic ordering under two vertical electric fields of $E_z = \pm 10$ mV/Å. Large spin splitting is clearly evidenced in the plots.

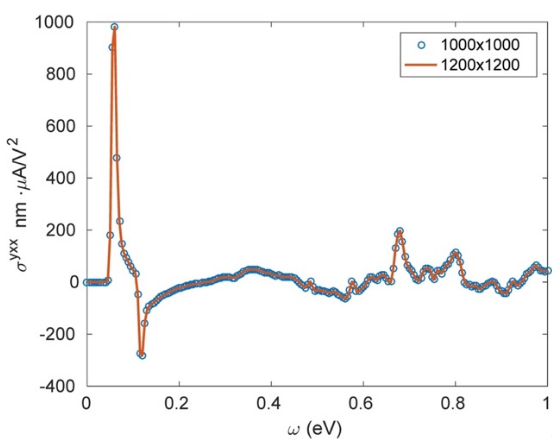

Figure S4 Convergence test of normal shift current susceptibility $\sigma_{\mathrm{NSC}}^{yxx}$ with respect to $\boldsymbol{k}$-point sampling in the first Brillouin zone of bilayer $MnBi_2Te_4$ with AFM-*z* magnetic ordering and under electric field of $E_z = -10$ mV/Å. A dense $\boldsymbol{k}$-point grid of 1000×1000×1 is enough to reach the convergence.